



RESEARCH ARTICLE

X-ray speckle reduction using a high-speed piezoelectric deformable mirror system

Shuai Yan¹, Hui Jiang^{1,2}, Zhisen Jiang¹, Dongxu Liang¹, Jianan Xie^{1,3}, Hai Zhu⁴, Guoyang Shu⁴, Ningyu Ben⁴, and Aiguo Li^{1,2}

¹Shanghai Synchrotron Radiation Facility, Shanghai Advanced Research Institute, Chinese Academy of Sciences, Shanghai, China

²Shanghai Institute of Applied Physics, Chinese Academy of Sciences, Shanghai, China

³Nankai University, Tianjin, China

⁴Huawei Technologies Co., Ltd, Shenzhen, China

(Received 16 October 2024; revised 15 December 2024; accepted 14 January 2025)

Abstract

An advanced deformable Kirkpatrick–Baez (K-B) mirror system was developed, equipped with high-speed piezoelectric actuators, and designed to induce beam decoherence and significantly enhance the quality of X-ray imaging by minimizing undesirable speckles in synchrotron radiation or free-electron laser facilities. Each individual mirror is engineered with 36 independent piezoelectric actuators that operate in a randomized manner, orchestrating the mirror surface to oscillate at a high frequency up to 100 kHz. Through *in situ* imaging single-slit diffraction measurement, it has been demonstrated that this high-frequency-vibration mirror system is pivotal in disrupting the coherent nature, thereby diminishing speckle formation. The impact of the K-B mirror system is profound, with the capability to reduce the image contrast to as low as 0.04, signifying a substantial reduction in speckle visibility. Moreover, the coherence of the X-ray beam is significantly lowered from an initial value exceeding 80% to 13%.

Keywords: decoherence; high-speed deformable mirror; speckle; X-ray

1. Introduction

In comparison to third-generation synchrotron radiation light sources, novel advanced light sources, such as X-ray free-electron lasers (XFELs) and diffraction-limited-ring synchrotron radiation facilities, provide significantly enhanced brightness and coherence. For instance, high-gain, high-repetition-rate XFELs^[1] operating in the self-amplified spontaneous emission (SASE) mode can generate coherent X-ray pulses with gigawatt-level power and femtosecond-level time intervals. These advancements are particularly beneficial for a range of X-ray techniques, such as time-resolved imaging^[2], ptychography^[3], projection holography^[4] and photon correlation spectroscopy^[5], facilitating cutting-edge scientific research. However, there are still some high-resolution imaging applications, especially

ultrafast full-field^[6] or projection imaging experiments, that need to avoid the presence of coherence when using such ultra-bright beams. The enhanced beam coherence also introduces the speckle phenomenon as background scattering, characterized by granular or noisy patterns resulting from the interference of coherent wavefronts with the surface irregularities of reflective or diffractive optics, beryllium or diamond windows and slit edges. Due to the unavoidable use of optical elements during the beam transmission process and the difficulty in controlling the surface shape of the elements to fully meet the Rayleigh criterion, these speckles cannot be avoided. Speckles degrade the signal-to-noise ratio or obscure the weak scattering from the sample, thereby diminishing image quality, contrast and resolution^[7]. In addition, speckles affect the precision of X-ray spectroscopy^[8] by altering the intensity distribution across the spectrum, leading to inaccuracies in determining elemental composition, chemical states and other spectroscopic parameters. Furthermore, the short, extremely intense X-ray pulses produced by XFELs are particularly susceptible to speckles.

Correspondence to: H. Jiang, Shanghai Synchrotron Radiation Facility, Shanghai Advanced Research Institute, Chinese Academy of Sciences, 239 Zhangheng Road, Pudong District, Shanghai 201204, China. Email: jiangh@sari.ac.cn; H. Zhu, Huawei Technologies Co., Ltd, Bantian, Long-gang District, Shenzhen 518129, China. Email: zhuhai12@huawei.com

Fluctuations in the X-ray pulse due to speckles compromise the consistency and reliability of time-resolved studies. Addressing the speckle issue is therefore crucial for the advancement and optimization of X-ray applications in scientific research.

Various strategies have been proposed to spatial decoherence in the visible light spectrum, including the use of moving diffusers^[9], polarization adjustments^[10], deploying multiple beams with varying angles or wavelengths^[11] and employing active deformable mirrors^[12,13] as part of optical decoherence schemes. In the realm of visible light projection, deformable mirrors have been instrumental in wavefront control^[14,15] and reducing speckle noise^[11,12] during imaging processes. These mirrors consist of numerous actuating elements, each capable of independently manipulating the mirror surface to induce the required deformation and correct wavefront aberrations. However, wavefront modulation in the X-ray domain necessitates superior surface control due to the shorter wavelengths involved. Grazing-incidence deformable mirrors were successfully employed in X-ray diffraction-limited focusing systems to correct aberrations to realize wavefront preservation^[16,17] or were used directly as bending actuators to form the desired surface profile of the mirror^[18,19]. This kind of mirror is capable of correcting the mirror's curvature with a high degree of precision, albeit with relatively slow response or closed-loop time at a refresh rate up to 1 kHz, due to the use of actuators functioning in the bimorph mode. In the X-ray domain, there have been previous studies that attempted to eliminate speckles or background noise in imaging by using a moving diffuser^[20,21] and altering the tilt angle of the mirror^[22]. However, these studies did not address high frequencies, making such devices insufficient for applications involving high-repetition-rate light sources, given that synchrotron radiation beams commonly operate in the megahertz (MHz)

frequency range, while XFELs often feature high repetition rates in the range of hundreds of kilohertz (kHz). Therefore, it is necessary to develop a high-frequency X-ray modulation device. One of the most popular types of two-dimensional X-ray imaging systems is the Kirkpatrick–Baez (K-B) piezoelectric deformable mirror. This technology enables the differentiation of individual speckles, ensures speckle homogeneity throughout the imaging exposure and allows for the deliberate disruption of coherent beam speckles under dynamic mirror surface conditions.

This paper presents the design and construction of a testing system specifically tailored for the decoherence of deformable mirrors. It encompasses an in-depth analysis and rigorous testing to explore the interplay between coherence and pivotal parameters, including vibrational frequency and displacement. These investigations are conducted through a combination of meticulous opto-mechanical design and extensive experimental procedures.

2. Deformable mirrors and *ex situ* measurements

2.1. Deformable mirrors

Our design integrates a series of stacked piezoelectric ceramic structures within the piston-type piezoelectric actuators. As depicted in Figure 1(a), these structures consist of 12 piezoelectric ceramic blocks, aligned along their longitudinal axis with a uniform gap of 2 mm separating each pair of blocks. Each ceramic block features an even distribution of six pairs of electrodes, with each electrode pair having a diameter of 1.5 mm on the bottom surface. Two adjacent pairs of electrodes are connected in parallel, sharing the same voltage potential. Consequently, this configuration results in a total of 36 independent voltage inputs for each mirror. These actuators exert controlled pushes and pulls

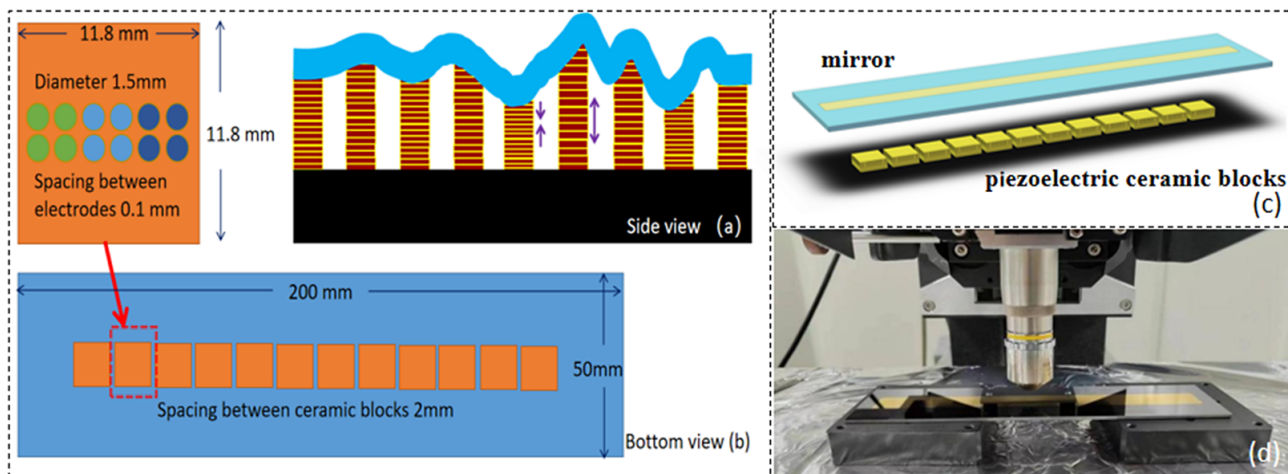


Figure 1. Schematic diagram of the modulation of surface shape by stacked piezoelectric piston actuators: (a) demonstration of piston-type piezoelectric actuators from the side view; (b) arrangement of actuator electrodes at the bottom of the mirror; (c) exploded view of the mirror; (d) mirror with the gold film measured by profile.

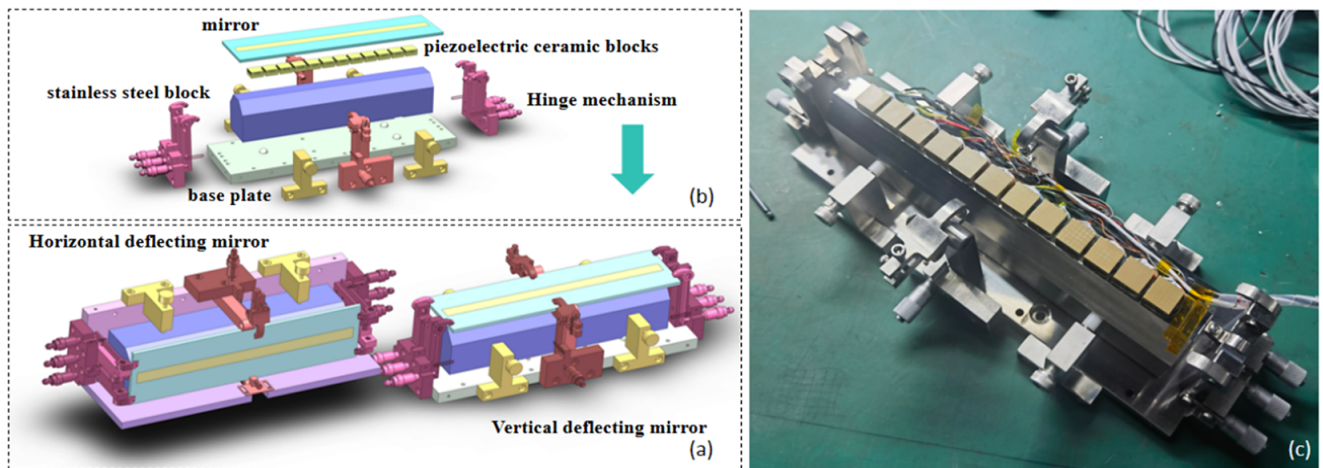


Figure 2. (a) Design drawing of the clamping and adjusting mechanism of the K-B mirror. (b) 3D exploded view of the vertical deflecting mirror. (c) Photograph of the piezoelectric actuators sticking on a thick stainless steel block.

on the mirror surface, thereby generating high-frequency vibrations, as illustrated in Figure 1(b). The piezoelectric ceramic material used is DM21S, characterized by a Poisson's ratio σ of 0.36, a Curie temperature T_c of 230°C, a Young's modulus E of 56 GPa, a piezoelectric constant d_{33} of 710×10^{-12} C/N and a frequency constant N_3 of 1500 Hz·m. Each stack of piezoelectric ceramic consists of $n = 70$ layers, with each layer having a thickness of 42 μm , which means the total electrode height is approximately 2.94 mm and the capacitance is about 50 nF. The displacement $\Delta L = nd_{33}U$ is directly proportional to the applied voltage U , thus allowing the theoretical maximum displacement of the stacked piezoelectric ceramics under no load and at a 50 V voltage to exceed 2 μm . Furthermore, the theoretical maximum resonant frequency of these ceramics can reach approximately 250 kHz.

The dimensions of each deformable mirror are 200 mm \times 50 mm \times 2 mm. As depicted in Figure 1(d), the ZYGO profiler assessed the root mean square (RMS) roughness of the silicon mirror surface and found that it was 0.37 ± 0.07 nm. To ensure a secure bond with the piezoelectric actuators, the mirrors' bottom surfaces were polished as well. An 80 nm layer of gold was deposited on the surface of each mirror to enhance reflectivity. Taking into account the mirror's slender profile, a 40 mm thick stainless steel block was seamlessly integrated into the clamping mechanism's design. Piezoelectric ceramics are adhered to the block surface using glue, creating a unified structure. The block's lower surface features a cone, a V-groove and a flat surface, which are designed to be supported by the base plate, ensuring the high stability of the mirror, as depicted in Figure 2(b). This block serves to support the thin mirror and counteract the effects of increased gravitational forces, thus ensuring stability during the high-frequency vibrational processes. The mirror adjustment mechanism is securely mounted to the stainless steel block via the clamping mechanism's base plate.

This clamping mechanism has been engineered to achieve submicrometer precision in both its pushing and bending operations, effectively correcting any minor distortions in the thin mirror that may arise due to clamping stress. Figures 2(a) and 2(b) present a three-dimensional design drawing of the mirrors and their respective mechanism systems. Figure 2(c) shows a photograph of the piezoelectric ceramics and stainless steel block prior to the mirror's attachment. Furthermore, the manipulator system enables precise adjustments in both position and angle, with capabilities extending into the submicrometer and submicrometer radian ranges, ensuring a high degree of accuracy and control.

2.2. High-voltage power supply

The stacked piezoelectric ceramic materials can be actuated by a high-power alternating current (AC) control power supply capable of delivering a maximum voltage of 50 V, allowing for frequencies up to 100 kHz. The voltage applied to any given actuator follows a sine function and adheres to a specific relationship equation:

$$U = U_{\max} \sin(2\pi ft + \varphi_0), \quad (1)$$

where U_{\max} represents the highest voltage that the power supply can apply, f denotes the activation frequency and φ_0 signifies the initial phase of the vibration. To effectively disrupt and modulate the coherence of the beam, the height deviation between adjacent surface shapes must surpass the Rayleigh criterion. This requirement is mathematically expressed through the following inequality:

$$\Delta h > \frac{\lambda}{8 \sin \theta}, \quad (2)$$

where λ is the wavelength and θ is the grazing-incidence angle of the mirror. Upon the application of a voltage, each actuator is capable of producing a protrusion with a Gaussian distribution of height across its original flat surface. The distribution of this protrusion's height can be mathematically expressed as follows:

$$\Delta h = \frac{AU}{\sqrt{\pi/2}\sigma_a} \exp\left(-\frac{2x^2}{\sigma_a^2}\right), \quad (3)$$

where A is the coefficient and σ_a is the half-width of the piezoelectric response function.

The multi-channel digital high-voltage control power supply is a sophisticated programmable system that comprises three interconnected components: a main control unit, a power transfer module and a power supply segment. Its logical schematic is depicted in Figure 3. The main control unit is at the heart of the system, featuring an advanced control chip coupled with a suite of peripheral circuits. The main control unit consists of the STM32F407 main control chip from STMicroelectronics, which has a main frequency of 168 MHz, an oscillation circuit and a reset circuit. The maximum serial peripheral interface (SPI) communication speed is 45 Mbit/s. The Ethernet communication chip model is W5500. The main control unit also integrates a user-friendly control panel, a digital-to-analog converter (DAC) for precision control and a robust network communication interface that ensures seamless connectivity. The DAC control chip uses the DAC81416 chip, which is produced by Texas Instruments and features an integrated internal reference voltage for 16 channels of 16-bit high-voltage output DACs. The power transfer section is engineered for efficiency and reliability, encompassing the DAC for signal conversion, a power conversion subsystem that manages energy flow, an

effective heat dissipation mechanism to maintain optimal operating temperatures and a durable chassis that houses the components. The power supply provides a stable and continuous flow of power to the entire system. The power supply is a direct current (DC) amplified high-voltage amplifier composed of a DAC+ interface and a conversion part.

2.3. Ex situ measurements

The amplitude and vibrational frequency of the mirror surface, upon the application of voltage to each actuator, were measured using a high-precision laser displacement measuring interferometer (Attocube IDS 3010/SMF, Figure 4(c)). As can be seen in Figures 4(a) and 4(b), a stainless steel frame was utilized to hold two mirrors in place during the measurement process. An optical fiber probe, mounted on a movable plate, was positioned over the surface of each mirror to facilitate measurements with a sensor resolution of 1 pm and a fast acquisition rate up to 10 MHz, as depicted in Figure 4(d). Figure 5(a) documents the amplitudes across different electrodes for both mirrors when a voltage of 50 V and a frequency of 30 kHz were applied to each actuator. The average amplitudes for the horizontal and vertical deflecting mirrors were measured to be 141.07 ± 50.44 and 166.62 ± 52.27 nm, respectively. Notably, the actuators located at the center and the edges of the mirrors demonstrated larger amplitudes. This variation is primarily likely due to the differences in force constraints imposed by the support of the stainless steel block and the clamping. Furthermore, Figure 5(b) captures the amplitudes as a function of varying actuation frequencies, up to 100 kHz, for the 17th actuator of the vertical deflecting mirror. When the driving frequency is 50 kHz, the maximum amplitude can reach

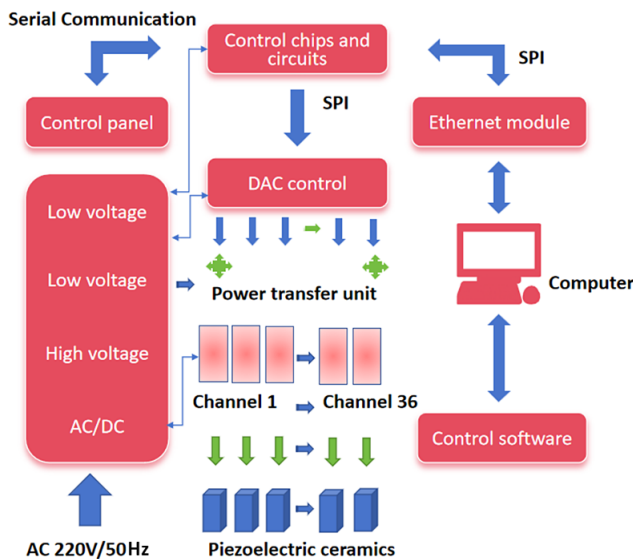


Figure 3. Logic diagram of the piezoelectric ceramic control process.

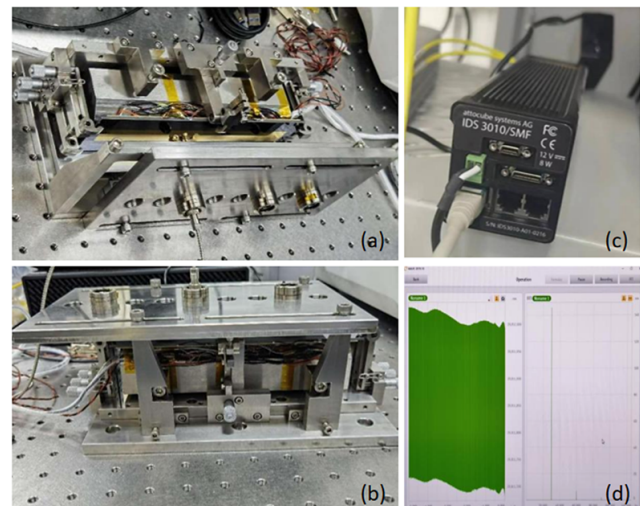


Figure 4. Ex situ experiments for (a) horizontal deflecting and (b) vertical deflecting mirrors by using (c) a laser interferometer with (d) the high-frequency data acquisition software IDS Feature: wave basic.

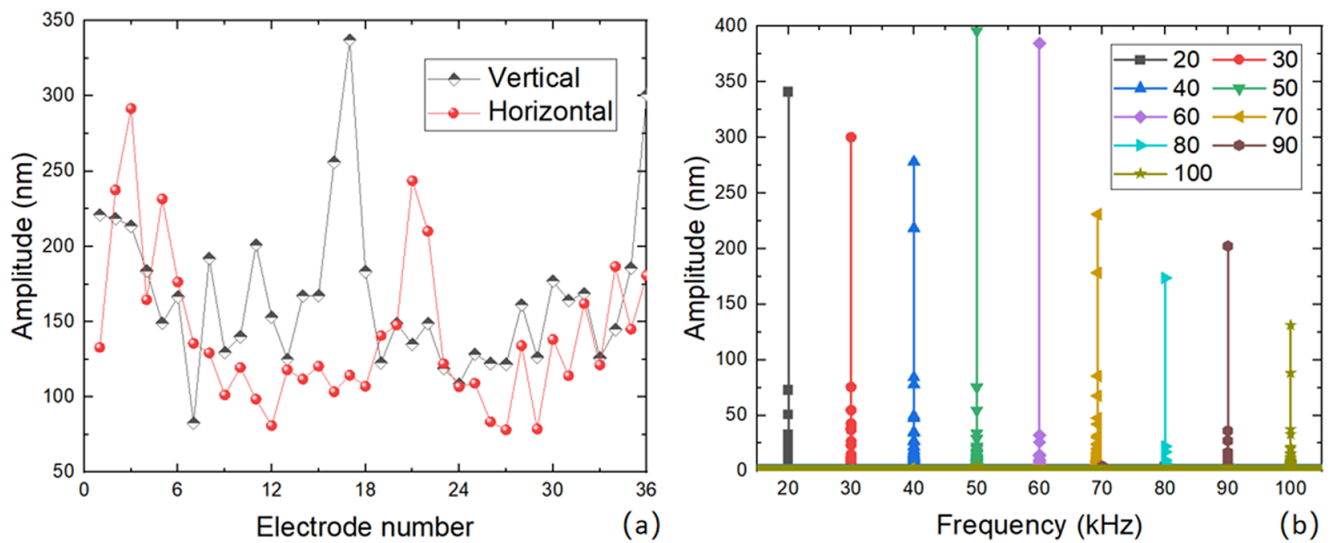


Figure 5. (a) The amplitude of mirror surfaces for different actuators for two mirrors and (b) the amplitude of the 17th actuator versus different frequencies.

400 nm. This data provides valuable insights into the behavior of the mirror system under different operational conditions. With the Fizeau interferometer, the surface profile of the entire high-speed deformation can be measured. For the average surface shape in the 1 second acquisition time for given actuation frequencies and voltages, the repeatability of less than 3 nm (RMS) was achieved in 10 minutes.

3. Modulation scheme and simulation

3.1. Modulation scheme

It is a well-established principle that to effectively deconstruct beam coherence and attain a substantial amplitude, the maximum voltage U_{\max} should be as large as possible. To reduce the phase difference within the divergence angle of the beam, a strategic approach is to assign markedly different initial phases to adjacent actuators. Beyond voltage and initial phase adjustments, varying the frequency at different positions across the mirror surface can further disrupt the correlation of the surface shape under various exposure conditions. Drawing on these premises, our simulation investigated three unique deformation modes to pinpoint the most effective adjustment mechanism for the deformable mirror surface, as illustrated in Figure 6. A pre-set phase was contemplated to address the challenge of implementing swift random phase adjustments in real-time by initiating the phase at a random value. In the case of mode 3, the frequency for every several actuators as a period was altered by a unique coefficient to disrupt the overall phase correlation.

Considering high-repetition-rate light sources can achieve frequencies up to the MHz range, and given that the mirror surface's deformation vibrations are of the order of tens of kHz, each vibrating surface may experience multiple pulse irradiations during high-repetition events. The simulation

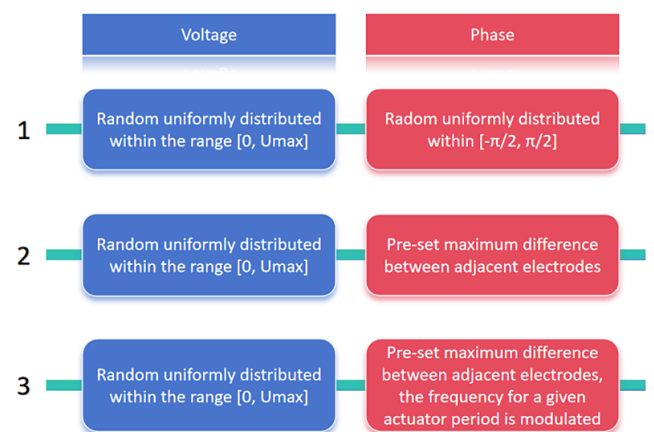


Figure 6. Three distinct deformation modes for actuator modulation.

for a single surface under different pulses can refer to the scenario of non-deformed vibration, and the actual number of collected data points should align with the actual frequency of the deformable mirror surface. For an imaging duration of approximately 1–10 seconds, this equates to 1–100,000 deformations. However, the data presented in this paper are capable of simulating, at most, 3000 iterations. Consequently, the effects attributed to the deformable mirror may be somewhat underestimated.

3.2. Simulation

In this simulation, a light source, such as the secondary light source shown in Figure 7, is emulated using a model based on an array of point light sources. Each cluster of pulse beams is arranged in a matrix array configuration on the XZ plane at the exit surface of the secondary source aperture (SSA). The two-dimensional normalized beam intensity dis-

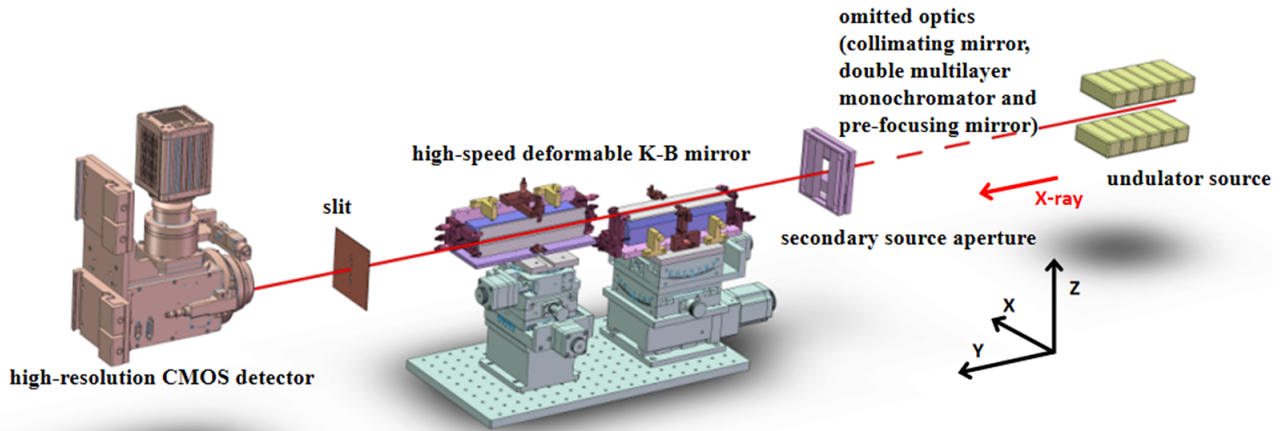


Figure 7. Schematic diagram of the optical path for single-slit diffraction.

tribution for these beam clusters adheres to a Gaussian distribution pattern:

$$I = \exp\left(-\frac{x^2}{2\sigma_x^2} - \frac{z^2}{2\sigma_z^2}\right), \quad (4)$$

where $\sigma_{x/z}$ represents the half-width of the beam intensity distribution at the secondary source. The size of each point light source corresponds to the actual physical dimensions. The phase at each position within the array is assigned a random value, uniformly distributed within the range of $[-\pi, \pi]$. For high-repetition-rate beams, each pulse is considered independent, meaning that the phase distribution array of the source for each pulse is completely different. The X-ray beams propagate freely along the Y -axis towards the K-B mirror. After two reflections off the K-B mirror, the beams ultimately reach either the slit or the detector. Given that the simulated optical path involves a fully coherent or partially coherent beam, the complex amplitudes of the spherical waves emitted from each point light source directly contribute to an amplitude superposition within the specified angular divergence. The intensity distribution at the detection surface is determined by calculating the modulus squared of the superposition of these complex amplitudes. The intensity distribution resulting from the superposition of these point light sources is considered to be an incoherent summation of their respective diffraction intensities. The minimum size of the speckle pattern has a specific relationship $s_{\min} = 1.22\lambda L/d$, where L is the distance from the mirror to the detector and d is the spot size. For a speckle pattern, contrast $C = \sigma/\bar{I}$ can be used to estimate the overall clarity of the speckles, with lower contrast indicating a disruption of beam coherence, where σ is the RMS intensity fluctuation and \bar{I} is the average intensity.

Throughout the propagation process, there are three distinct steps of free space propagation: the first from the light source to the vertical deflection mirror, the second from the vertical deflection mirror to the horizontal deflection mirror and the third from the horizontal deflection mirror to the detector. For each of these propagation steps, the Huygens–Fresnel diffraction formula is applied to accurately model the behavior of the light waves:

$$U(P_1) = \frac{1}{j\lambda} \iint_{\Sigma} U(P_0) \frac{\exp[jk(r_{01})]}{r_{01}} \cos(\theta_{01}) ds. \quad (5)$$

Among them, $U(P_1)$ represents the complex amplitude at observation point P_1 , $U(P_0)$ represents the complex amplitude at point P_0 , s is the facet at the diffraction surface Σ , j is an imaginary unit, k is the wave vector of the beam, r_{01} represents the distance between points P_0 and P_1 and θ_{01} represents the angle between the line connecting P_0 and P_1 and the normal at surface P_0 .

Single-slit diffraction^[23,24] serves as a straightforward method for measuring the coherence of a beam. This process involves the interference and subsequent divergence of beams as they encounter an aperture that is similar in size to the beam's wavelength. The type of diffraction pattern observed – whether Fresnel or Fraunhofer fringes – depends on the slit-to-detector distance when X-ray photons traverse a slit of width a . The coherence of the beam at a specific point can be inferred from the visibility of these fringes. The visibility of the central fringe, in particular, can be determined using the following expression, which relates to the coherent length of the beam:

$$V = V_0 \exp\left(-\frac{a^2}{8l_c^2}\right) = \frac{I_{\max} - I_{\min}}{I_{\max} + I_{\min}}, \quad (6)$$

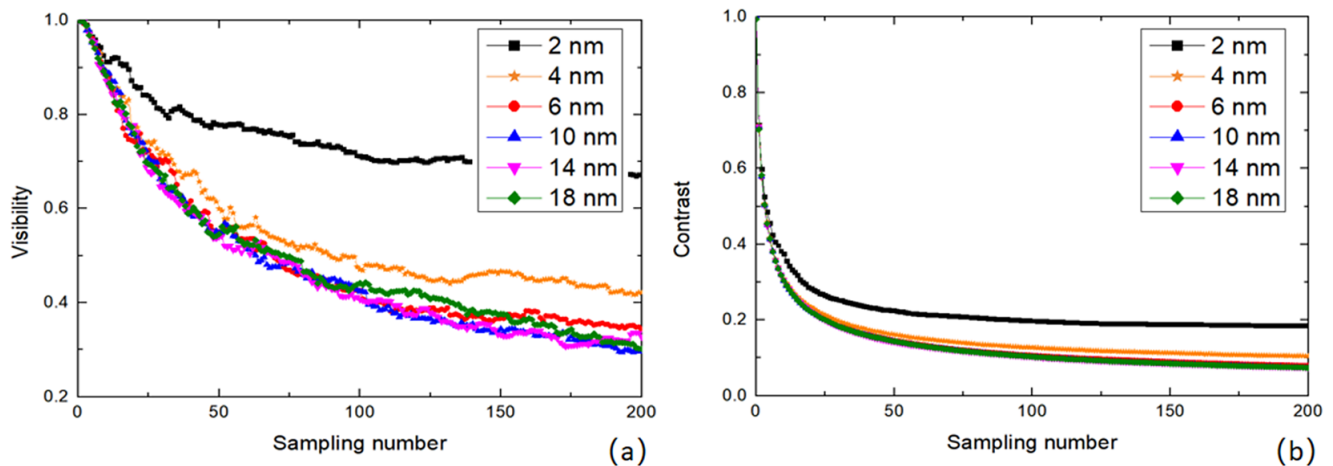


Figure 8. The (a) visibility and (b) contrast of imaging at different PV vibrational amplitudes from 2 to 18 nm vary with the increase in the sampling number.

where I_{\max} and I_{\min} are the local maximum and minimum intensities, respectively, near the center fringe, l_c is the beam transverse coherence length and V_0 is the visibility of the central fringe in the case of point source, given by Ref. [20].

The first simulation aimed to study the effectiveness of the deformable mirror scheme. The mirror shape actuated by 36 completely random voltages with different maximum values and the visibility and contrast of the reflective imaging were used to evaluate the beam coherence. Figure 8 illustrates the variations in visibility and contrast of two-dimensional speckle patterns under the influence of different amplitudes of random vibration. When the amplitude of vibration exceeds a peak-to-valley (PV) value of 4 nm, there is a marked disruption in coherence, leading to a notable reduction in both visibility and contrast. The results were in agreement with the Rayleigh criterion. Upon reaching a PV amplitude of 18 nm for the random vibration of the surface, after accumulating 600 samples, the contrast can be diminished to as low as 0.04, while the visibility can be reduced to 0.18.

We conducted a comparison of the local speckle patterns under three distinct operational modes: no mirror vibration, random vibration with random phase and random vibration with a pre-set phase as described in the modulation scheme. This comparison was made after acquiring 1, 5, 100 and 500 exposure samples, respectively. Figure 9 presents a comparative analysis of the contrast curves for several deformable mirror vibration strategies following 500 samples. After long-term exposure, speckle patterns cannot be entirely eliminated in the absence of vibration, and even when the phases of the pulse beams vary, the contrast is at best reduced to 0.33. However, employing a deformable mirror can significantly diminish the contrast of the speckles to below 0.06. It appears that the rate of speckle homogenization increases with the number of random parameters

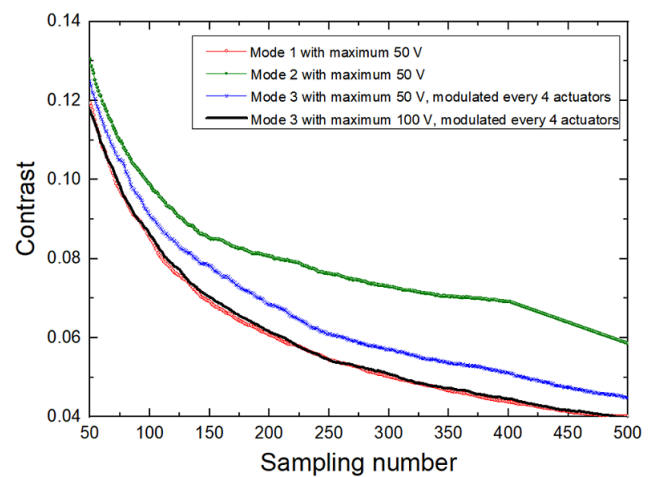


Figure 9. Comparison of the contrasts with different modulation schemes.

introduced into the system. Mode 1 described in Figure 6 can diminish the contrast to below 0.04 after 500 exposures. Mode 3 was proved to be very effective to reduce contrast compared to mode 2. By increase the voltage, mode 3 can achieve the same effect of mode 1. As can be seen in Figure 10(b), after accumulating 3000 vibration samples, the system with random vibration and a pre-set phase, along with partial frequency modulation, shows a visibility approaching 0.08 and a contrast that can be lowered to an exceptionally low value of 0.02. The trend in the data suggests that these values can continue to decline.

Figure 10(a) depicts the initial shape of the light spot following 5, 100 and 500 times of homogenization. Under the current modulation mode, while the speckle characteristics undergo significant changes, the position and general shape of the light spot remain essentially unchanged. Upon completion of 500 homogenization cycles, a marked reduction of the speckle contrast is observed, culminating in a light spot that is notably more uniform in appearance.

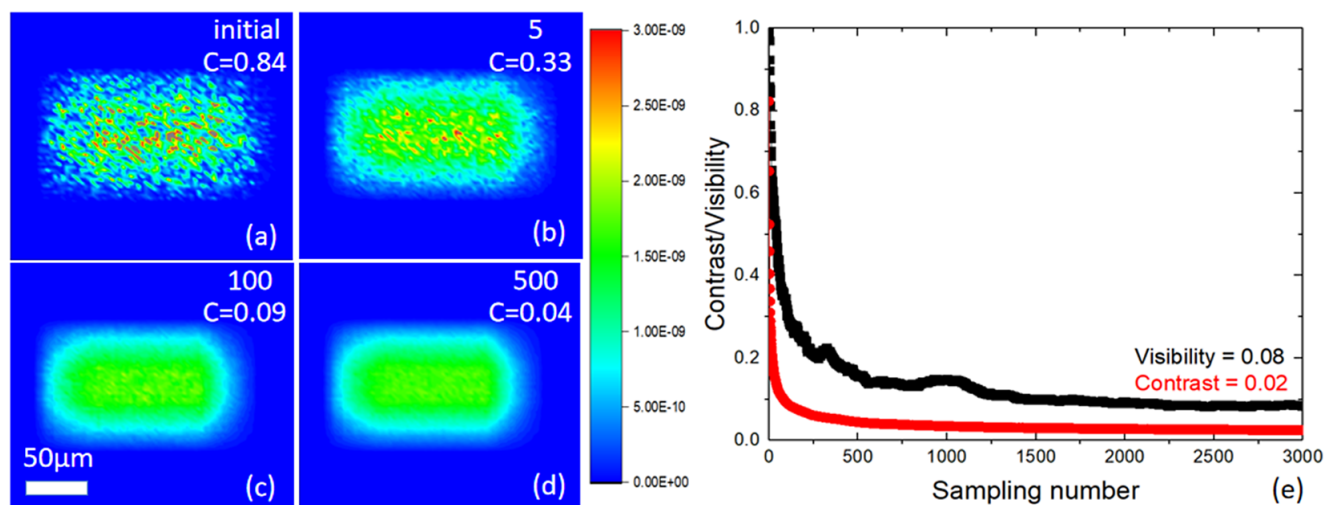


Figure 10. Comparison of the (a) initial light spot and the spot after (b) 5, (c) 100 and (d) 500 times of homogenization and their contrasts; (e) the visibility and contrast with the increase of sampling number.

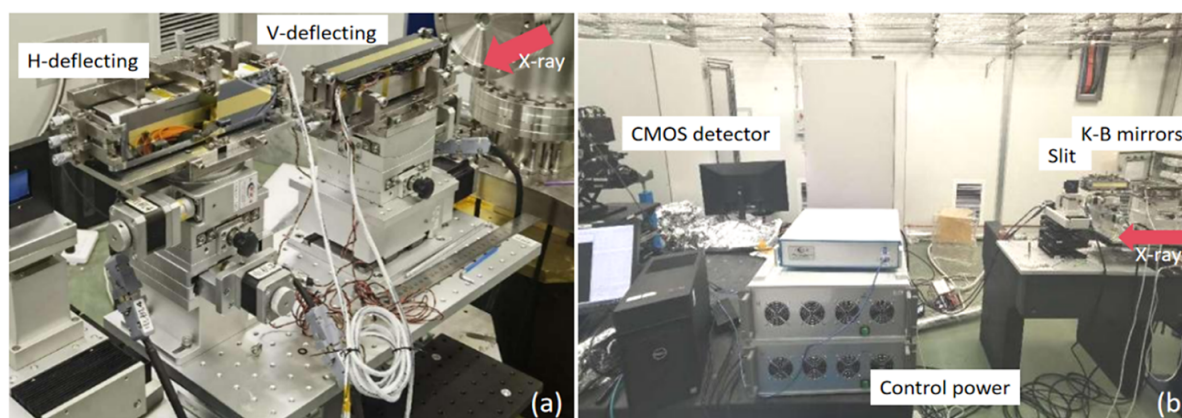


Figure 11. Photos of (a) the K-B system and (b) the overall experimental layout.

4. *In situ* experiments

The *in situ* measurement was carried out at the hard X-ray nanoprobe beamline (BL13U) with an operational energy of 10 keV. The comprehensive layout of the beamline is detailed in Refs. [17,25]. Figure 7 displays the schematic diagram for an *in situ* single-slit diffraction experiment, which is engineered to induce beam decoherence. In the context of the imaging experiment, the slit was removed. The distance spanning from the pre-focusing mirror to the SSA is established at 23 m. The slit opening of the SSA was $50\ \mu\text{m}$ (H) \times $20\ \mu\text{m}$ (V) to keep a relatively high degree of coherence. The K-B mirror system is situated approximately 67 m downstream from the SSA. The grazing-incidence angle for each mirror was 2.1 mrad. A four-bladed slit is positioned 400 mm downstream of the central region of the K-B mirror system. Subsequently, a microscope objective lens system with a $50\ \mu\text{m}$ thickness YAG:Ce (yttrium aluminum garnet activated by cerium) scintillator, integrated with a complementary metal-oxide-semiconductor (CMOS)

camera, is positioned 1872 mm downstream from the slit. The detector is equipped with a pixel size of $0.65\ \mu\text{m}$, arrayed in a 2048×2048 pixels grid. The exposure time for each image was 10 seconds. The actuation frequency of all channels was 30 kHz.

Figure 11 displays the actual image from the *in situ* test. Under consistent experimental conditions, the diffraction fringes were measured multiple times, yielding curves that are in good agreement with an average deviation of 0.40%. Figure 12 illustrates the application of different maximum random voltages to the mirror, which is actuated by 36 channels. The single-slit diffraction fringe patterns evolve through various phases with an initial setting. The slit width for the single-slit diffraction is set at $85\ \mu\text{m}$ in both horizontal and vertical directions. In this scenario, the theoretical visibility V_0 in Equation (6) is 0.289. As the random maximum voltage applied increased, the significant decrease of the visibility of the diffraction fringe can be observed. There are several ripples in the periphery apart from the vicinity of the slit opening. This was caused by

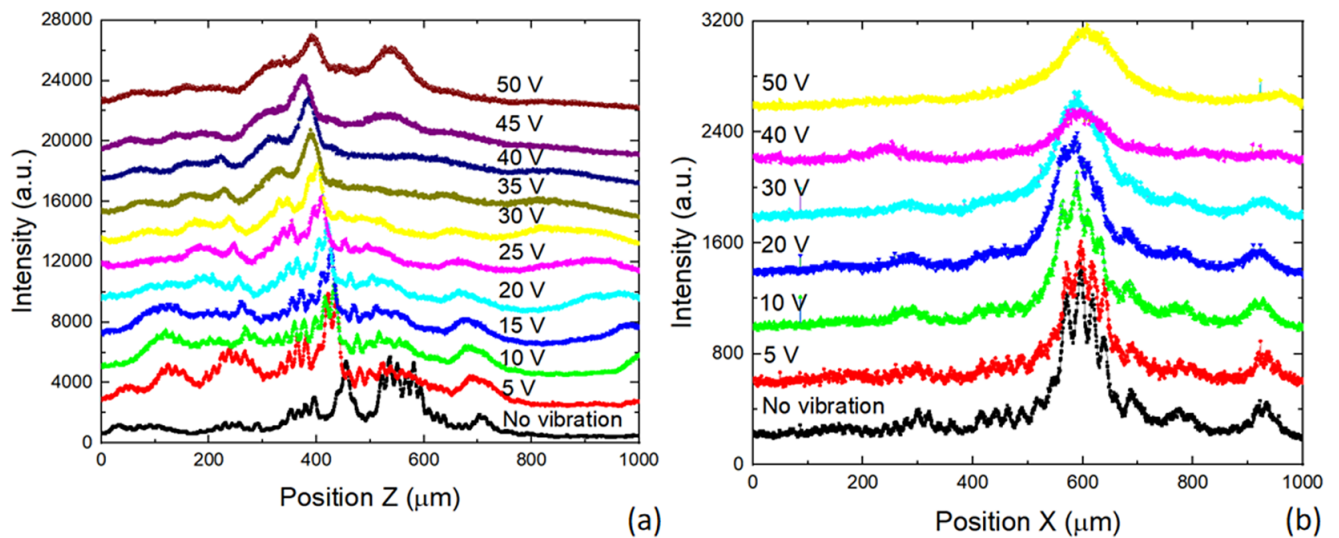


Figure 12. Single-slit diffraction along the (a) vertical and (b) horizontal directions with the increase of the action voltage.

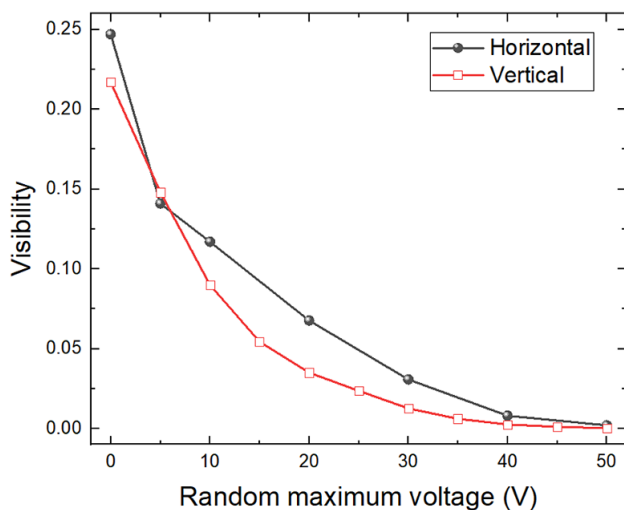


Figure 13. Visibility of the single-slit diffraction with the increase of the random maximum voltage.

the partial oblique incidence of the beam due to shape errors.

Figure 13 compares the changes in fringe visibility at the central region of the diffraction pattern under different maximum random voltages. The findings indicate that the visibility drops from over 0.20 without vibration to around 0.05 at 20 V. Furthermore, the streaks within the spot are nearly eliminated when the vibration is increased to 50 V, signifying that the coherence has been effectively disrupted. Based on Equation (6), the calculated transverse coherence lengths are found to decrease from 76 to 13 μm in the horizontal direction and from 56 to 11 μm in the vertical direction. Consequently, the degree of coherence is reduced from over 80% to approximately 13%.

The CMOS high-resolution imaging system is also capable of directly capturing the reflected beam's spot and subsequently calculating the contrast of the beam speckle, as

depicted in Figures 14(a)–14(d). The test results presented in Figure 14(b) demonstrate a significant reduction in imaging contrast with an increase of voltage. Specifically, the contrast is observed to decrease by 0.037 at the maximum voltage of 50 V.

5. Conclusions

We have successfully demonstrate a high-speed piezoelectric deformable K-B mirror system that can rapidly change the mirror shape, modulate the X-ray beam uniformity and reduce the coherence. The high-frequency vibration's frequency and amplitude were confirmed using a laser interferometer that recorded data at a 10 MHz acquisition rate. The amplitude of the vibrations exceeded 140 nm, while the frequency reached 100 kHz. At the hard X-ray nanoprobe beamline of the SSRF (Shanghai Synchrotron Radiation Facility), an *in situ* test was conducted. The modulation of the beam's coherence characteristics under high-frequency random vibration was confirmed, and single-slit diffraction and imaging techniques were used to verify the influence of vibration on the visibility of diffraction fringes and the speckle contrast in imaging, respectively. The results demonstrated that the equipment met the requirements of decoherence and could obtain a contrast better than 0.04.

The simulations and experiments prove the effectiveness of X-ray high-speed piezoelectric deformable mirrors on beam decoherence and speckle reduction. The maximum vibrational frequency has been increased to 100 kHz, which nearly satisfies the high-speed imaging experiments at XFELs with a high repetition rate. In the future, it may be increased to MHz to meet the experimental requirements at the picosecond level. However, the mirror must be made extremely thin in order to achieve a very high vibrational frequency and amplitude, which causes significant undesirable shape error when the mirror is

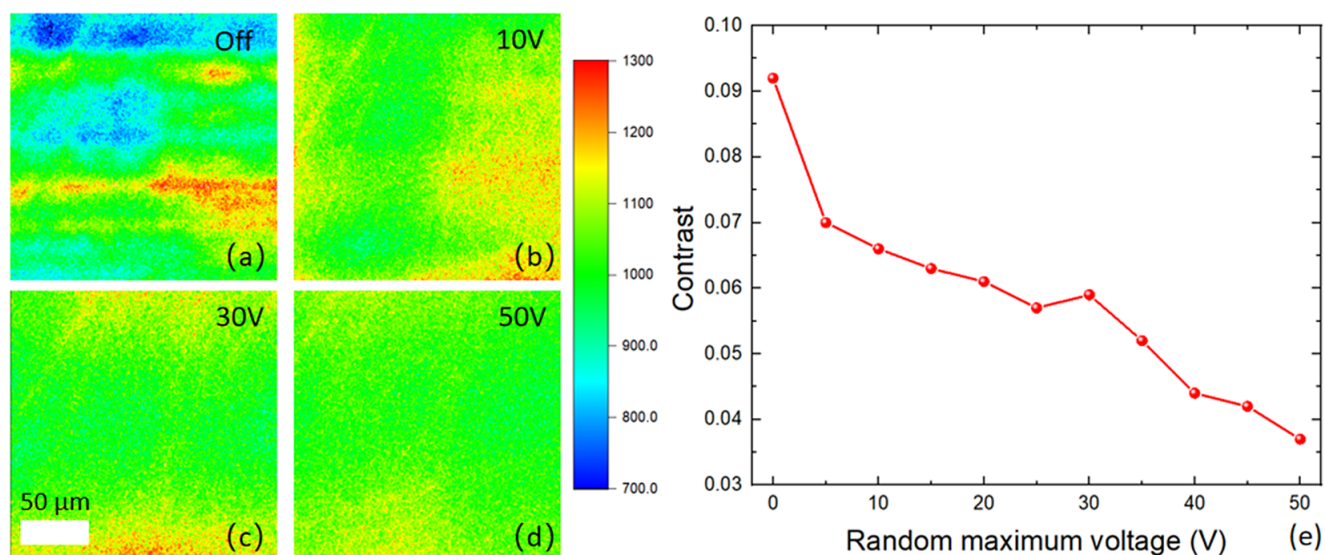


Figure 14. Imaging with the speckles while (a) no voltage applied and maximum (b) 10 V, (c) 30 V and (d) 50 V applied; (e) variation in the contrast of the images with the increase of the maximum voltage.

clamped and supported. These mirror form errors cause distortion or undesired speckle fringes. This is an urgent issue that will eventually need to be resolved. Better mirror modulation strategies must also be suggested in order to fully deconstruct the beam coherence. Another key technological issue is to build a novel piezoelectric actuator structure with a higher resonance frequency and create a power supply that can support a higher activation frequency and voltage, both of which are necessary to fully satisfy the demand for greater repetition rates for specific dynamic experiments.

Acknowledgements

This work was financially supported by the National Key Research and Development Program of China (Grant No. 2023YFA1608604), the National Natural Science Foundation of China (Grant Nos. 12175294 and 12235011) and the Natural Science Foundation of Shanghai Municipality (Grant No. 21ZR1471500).

References

1. M. Altarelli, *High Power Laser Sci. Eng.* **3**, e18 (2015).
2. S. M. Bak, Z. Shadik, R. Lin, X. Q. Yu, and X. Q. Yang, *NPG Asia Mater.* **10**, 563 (2018).
3. F. Pfeiffer, *Nat. Photonics* **12**, 9 (2018).
4. W. H. Zhang, J. L. Dresselhaus, H. Fleckenstein, M. Prasciolu, M. Zakharaova, N. Ivanov, C. F. Li, O. Yefanov, T. Li, D. Egorov, I. de G. Aquino, P. Middendorf, J. Hagemann, S. Shi, S. Bajt, and H. N. Chapman, *Opt. Express* **32**, 30879 (2024).
5. T. Konstantinova, L. Wiegart, M. Rakitin, A. M. DeGennaro, and A. M. Barbour, *Sci. Rep.* **11**, 14756 (2021).
6. S. Matsuyama, S. Yasuda, J. Yamada, H. Okada, Y. Kohmura, M. Yabashi, T. Ishikawa, and K. Yamauchi, *Sci. Rep.* **7**, 46358 (2017).
7. R. Cerbino, L. Peverini, M. A. C. Potenza, A. Robert, P. Bosecke, and M. Giglio, *Nat. Phys.* **4**, 238 (2008).
8. H. T. Lemke, C. Bressler, L. X. Chen, D. M. Fritz, K. J. Gaffney, A. Galler, W. Gawelda, K. Haldrup, R. W. Hartsock, H. Ihee, J. Kim, K. Kim, J. H. Lee, M. M. Nielsen, A. B. Stickrath, W. Zhang, D. Zhu, and M. Cammarata, *J. Phys. Chem. A* **117**, 735 (2013).
9. S. Kubota and J. W. Goodman, *Appl. Opt.* **49**, 4385 (2010).
10. S. Mousavi, E. Plum, J. Shi, I. Nikolay, and I. Zheludev, *Sci. Rep.* **5**, 8977 (2015).
11. N. E. Yu, J. W. Choi, H. Kang, D. K. Ko, S. H. Fu, J. W. Liou, A. H. Kung, H. J. Choi, B. J. Kim, M. Cha, and L. H. Peng, *Opt. Express* **22**, 3547 (2014).
12. T.-K.-T. Tran, X. Chen, Ø. Svendsen, and M. H. Akram, *Opt. Express* **22**, 11152 (2014).
13. H. A. Chen, J. W. Pan, and Z. P. Yang, *Opt. Express* **25**, 18140 (2017).
14. M. Booth, *Light Sci. Appl.* **3**, e165 (2014).
15. Z. Zhou, J. F. Huang, X. Li, X. F. Gao, Z. Y. Chen, Z. F. Jiao, Z. H. Zhang, Q. M. Luo, and L. Fu, *PhotonIX* **3**, 13 (2022).
16. H. Mimura, S. Handa, T. Kimura, H. Yumoto, D. Yamakawa, H. Yokoyama, S. Matsuyama, K. Inagaki, K. Yamamura, Y. Sano, K. Tamasaku, Y. Nishino, M. Yabashi, T. Ishikawa, and K. Yamauchi, *Nat. Phys.* **6**, 122 (2010).
17. H. Jiang, J. N. Xie, Y. He, Z. S. Jiang, D. X. Liang, H. N. Yu, and A. G. Li, *Opt. Express* **32**, 13597 (2024).
18. S. G. Alcock, I. Nistea, V. G. Badami, R. Signorato, M. Fusco, L. F. Hu, H. Wang, and K. Sawhney, *Optica* **10**, 172 (2023).
19. N. X. Tian, H. Jiang, J. N. Xie, S. Yan, D. X. Liang, and Z. S. Jiang, *J. Synchrotron Rad.* **31**, 10 (2024).
20. Y. Y. Kim, L. Gelisio, G. Mercurio, S. Dziarzhytski, M. Beye, L. Bocklage, A. Classen, C. David, and O. Y. Gorobtsov, *Phys. Rev. A* **101**, 013820 (2020).
21. S. C. Irvine, K. S. Morgan, Y. Suzuki, K. Uesugi, A. Takeuchi, D. M. Paganin, and K. K. W. Siu, *Opt. Express* **18**, 13478 (2010).
22. M. Eddah, H. Markötter, B. Mieller, M. Sintschuk, J. Beckmann, and G. Bruno, *J. Synchrotron Radiat.* **31**, 1551 (2024).
23. V. Kohn, I. Snigirev, and A. Snigirev, *Phys. Rev. Lett.* **85**, 2745 (2000).
24. H. Jiang, S. Yan, H. Wang, Y. Zheng, Z. H. Dong, and A. G. Li, *Appl. Phys. B* **122**, 271 (2016).
25. Y. He, H. Jiang, D. Liang, Z. S. Jiang, H. N. Yu, H. Wang, C. W. Mao, J. Xie, and A. G. Li, *Nucl. Sci. Tech.* **35**, 121 (2024).